Title

Neurons alter endoplasmic reticulum exit sites to accommodate dendritic arbor size

Author List

Ruben Land[1], Richard Fetter[2], Xing Liang[1], Christopher Tzeng[2], Kang Shen[1,2]

Affiliations

1. Department of Biology, Stanford University
2. Howard Hughes Medical Institute, Stanford University

Abstract

Nervous systems exhibit dramatic diversity in cell morphology and size. How neurons regulate their biosynthetic and secretory machinery to support different cell sizes is not well understood. Endoplasmic reticulum exit sites (ERESs) are essential for maintaining secretory flux, and are required for normal dendrite development.[1] However, it is unknown how neurons of different size regulate the number of secretory structures to accommodate morphogenesis. In *C. elegans*, we find that ERES number is strongly correlated with the size of a neuron's dendritic arbor. The elaborately branched sensory neuron, PVD, has especially high ERES numbers in its soma. PVD establishes its high ERES number rapidly after birth, actively maintains ERES number as PVD grows and matures. The initial high number of ERES in PVD is driven by asymmetric cell division producing a large cell size at birth. Subsequent maintenance of ERES number requires the cell fate transcription factor MEC-3 and *C. elegans* TOR (*ceTOR/let-363*). This *ceTOR/let-363* pathway integrates nutrient availability to coordinate ERES number with soma size and dendritic expansion. Our results are consistent with a model in which transcription factors, master metabolic regulators and nutrient availability coordinate to specify developmental parameters including soma size, ERES number and dendrite size, which together determine neuronal cell fate.

Introduction

Neurons exhibit a large diversity in morphology and size. A single nervous system contains small neurons with simple morphology and very large neurons with extremely complex neurites. How neurons adjust their biosynthetic activity to match their morphology and size is not well understood. It is well known that cell types with secretory functions such as pancreatic acinar cells, have expanded rough ER and Golgi apparatus[2]. Work in secretory cells and mammalian cell lines demonstrate that early secretory organelle size and number is associated with changes in secretory cargo load[3–5]. However, it is not currently known how post-mitotic neurons of different types regulate early secretory organelle structure to accommodate divergent cell sizes *in vivo*.

Caenorhabditis elegans hermaphrodites have 302 neurons of widely varying size and complexity, many of which can be genetically manipulated on the individual cell level. In addition, the transparent *C. elegans* allows for visualization of secretory organelle formation and dynamics within a single neuron throughout its development *in vivo*. The vast majority of *C. elegans* neurons a have simple cell morphology with 1 or 2 unbranched neurites. However, the multimodal sensory neuron PVD develops an expansive dendritic arbor with over 150 terminal branches that cover the majority of the worm's body.

Accurate measurement of secretory flux is technically challenging in an intact animal. Examination of ER-exit sites (ERESs) provides several advantages for assessing the structure and activity of the secretory system *in vivo*. ERESs are central nodes of the secretory pathway, providing the earliest checkpoint for transport of correctly folded proteins through ER to subsequent secretory organelles[6]. ERES size and number have been shown to change with secretory flux[5], and their function is required for normal dendrite morphology in *Drosophila* neurons[1]. In addition, ERESs can be fluorescently labeled, as their molecular components are well known and highly conserved[6,7]. Finally, *C. elegans* ERESs can be visualized with fluorescence light microscopy, and quantified due to their round, distinct punctate appearance[8].

In this study, we characterized ERES number in a subset of *C. elegans* neurons of different sizes and complexities. We report that neurons with larger dendrites had significantly higher ERES numbers. In cell fate mutants that alter dendrite size, we observed a strong correlation between ERES number and dendrite size. PVD, the largest cell examined and *C. elegans'* largest neuron, displayed the highest number of ERESs. We found that high ERES number in PVD is established rapidly after neuron birth before neurite outgrowth, and maintained throughout development. Establishment of high ERES number is driven by asymmetric cell division and resultant large cell size at birth. Maintenance of ERES number is regulated by the transcription factor MEC-3 and *C. elegans* TOR (*ceTOR/let-363*), and is coordinated with the nutrient availability. Finally, we observed that *C. elegans* starvation during early development caused a reduction in PVD ERES number. Notably, starvation after PVD maturity had little to no impact on ERES number. These data support the notion that transcription factors and master growth regulators coordinate soma size and ERES number to accommodate dendrite size, and raises the possibility that asymmetric cell division can help to initiate differing metabolic capacities.

Results

To understand the molecular mechanisms that generate the morphological diversity of neurons, we postulated that biosynthetic and membrane trafficking pathways are tuned to neuron size and complexity. We tested this idea by visualizing the ER-exit sites (ERESs) in neuronal types with different morphological complexity. We labelled neuronal ERESs by constructing an endogenous fluorescent tag of ERES protein SEC-16 (GFP::SEC-16), which showed discrete, round puncta that are largely restricted to cell bodies (Fig. 1a). With this tool, we observed that neurons with larger, more complex morphologies have significantly higher numbers of ERESs in their cell bodies or somas (Fig. 1). Touch receptor neurons AVM and PVM, each with fewer than 5 terminal neurite branch points, typically have three to four distinct somatic ERESs. In contrast, significantly higher numbers of ERESs are found in the somas of FLP and PVD, each of which have highly branched dendrites with dozens of terminal neurite branch points (Fig. 1a, b, c). PDE, a smaller sensory neuron within the same lineage as PVD, has fewer Golgi and ERESs than PVD. Comparing individual FLP and PVD neurons, we also found a trend that cells with higher branch numbers have more ERESs (Fig. 1c). To validate these results using electron microscopy (EM), we performed serial sectioning EM reconstruction of PVD and PDE cell soma. From these EM images we indeed observed discrete ER exit sites that are associated with a Golgi apparatus (Fig. 1d-g).

In order to test the importance of ERES function for dendrite growth in PVD, we expressed a dominant negative version of the ERES protein SAR-1 (SAR-1DN) specifically in PVD. SAR-1 is a small GTPase required for protein trafficking from ER to Golgi[9,10]. Overexpression of SAR-1DN severely disrupts dendrite growth in PVD (Fig. 1h), suggesting that ERES function is critical for dendrite growth and branching, resulting in a dramatic reduction of the 3° and 4° branches (Fig. 1h).

To further understand the relationship between dendritic branch complexity and ERES numbers, we examined transcription factor mutants that disrupt dendritic development and have reduced dendritic complexity. MEC-3 and UNC-86 are transcription factors that affect many aspects of PVD cell fate including dendrite growth. In *mec-3(e1338)* or *unc-86 (e1416)* mutants, PVD loses nearly all of its dendrites (Fig. 2a). Interestingly, we also find a corresponding reduction in ERES number in PVD soma in these mutants. We also examined a cell fate mutant with increased dendritic complexity. Wild-type (WT) AVM has simple neurite morphology. In transcription factor *ahr-1(ju145)* mutants, AVM becomes a cell with a PVD-like dendritic arbor, cAVM (Fig. 2c). Notably, cAVMs also have much higher ERES

numbers (Fig. 2d). These results indicate that transcription factors might specify ERES numbers as part of cell fate decisions.

A central question emerges from the above observations: How do large neurons establish and maintain high ERES abundance in coordination with a large dendrite? We chose to explore this question more thoroughly in PVD, given its large dendritic arbor and unusually high ERES number. Two simple models for how PVD might generate high ERES numbers are the: 1) feedback and 2) cell fate models. In the feedback model, as neurites develop, PVD's surface area expands dramatically and the peripheral demand for proteins and membrane increases, triggering signals that propagate back to the soma to upregulate the number of secretory organelles. Alternatively, in the cell fate model, ERES abundance is "hard-coded," established early in development via terminal cell fate pathways regardless of feedback from growing dendrites. The feedback model makes two key predictions: 1) Normal dendrite growth is required to promote PVD's high abundance of secretory organelles, and 2) PVD is born with initially fewer ERES, which increase in number during dendrite outgrowth. In contrast, the fate model makes two predictions that distinguish it from the feedback model: 1) Secretory organelle abundance is independent of normal dendrite outgrowth, and therefore, 2) ERES number may be established before neurite outgrowth and maintained at consistent levels throughout dendrite development.

To test the first prediction of each model, we disrupted several factors that are critical for PVD dendrite guidance[11–13]. Perturbation of these guidance receptors severely disrupt PVD dendrite morphology but do not alter the number of early secretory organelles (Fig. S1). These results suggest that normal dendrite outgrowth is not required for high organelle abundance, providing evidence against a feedback model that requires normal dendrite morphology.

To test the second predictions of the feedback and fate models, we conducted time-lapse and time course experiments of PVD development to determine when ERES number is established, and whether there are changes in ERES number over time during neurite outgrowth (Fig 3). Time-lapse imaging of ERESs during PVD birth requires an ERES marker with three key characteristics: 1) Endogenous expression, to avoid overexpression artifacts, 2) specificity, to allow identification of neurons of interest and, 3) Reliable expression that turns on early enough in development to be seen during PVD birth. There is a natural trade-off between specificity and early expression because the earlier within a cell lineage that an endogenous marker is turned on, the broader the expression will be in subsequent terminally differentiated cells. It was therefore crucial to identify a promoter that was able to turn on expression early enough to visualize ERESs during PVD birth, but late enough to avoid background expression that would prohibit identification of ERESs in PVD. In order to meet these criteria, we built a FLP-ON system for endogenous labeling of the ERES-associated protein SEC-16, in which the GFP::SEC-16 fusion protein is turned on by a flippase under the control of early pan-neuronal promoter p*lin-32*.

With this toolset, we were able to directly observe ERES emergence during PVD birth and understand how ERES number is established. From these time-lapse experiments, we identify two distinct phases of ERES dynamics during PVD development. Phase I occurs during and immediately after cell division. Phase II spans an expanded period of time after Phase I. During cell division, we observe that GFP::SEC-16 became diffusely localized within the soma. As mitosis concludes, GFP::SEC-16 rapidly coalesces into puncta within three minutes of cytokinesis (Fig. 3a). These puncta undergo a brief period of consolidation within the first several minutes of PVD birth, establishing a high number of ERESs (in comparison to other neurons) before neurite outgrowth. This rapid establishment of high ERES numbers is consistent with the notion that ERES number is determined by cell fate, and *in*consistent with prediction 2 of the feedback model (Fig. 3b, c, d). These results indicate that high ERES number is established very early in PVD development and does not require feedback from dendrite outgrowth.

Subsequently, during Phase II, ERES number remains at consistently high levels throughout PVD development (Fig. 3d). It is an interesting question whether the ERES structures, once established during Phase I, are static structures that are fixed throughout Phase II during neurite outgrowth, or whether the consistent ERES number during Phase II is actively maintained. The continuous membrane flow through ERESs seems to be at odds with the static ERES model. In next sets of experiments, we seek to address two central questions that emerge from the above observations with respect to the two phases of ERES dynamics: 1) How are high ERES numbers initiated (Phase I) in PVD?, and 2) Are high ERES numbers in Phase II actively maintained during PVD neurite outgrowth, and if so, how?

To address how PVD establishes high ERES numbers during Phase I, we closely examined ERES number during PVD birth. Consistent with previous findings, our time-lapse imaging showed that PVD is born as the larger daughter cell of an asymmetric cell division[14] (Fig. 3b). PVD's smaller sister ("PVDsis") is eventually eliminated via apoptosis[14] (data not shown). Time-lapse imaging also showed that once GFP::SEC-16 rapidly coalesces into puncta, the initial ERES number in PVD is consistently higher compared to PVDsis (Fig. 4a). We hypothesized that this asymmetric cell division is important for unequal distribution of cytoplasm, membranes, and ERES components, and may be responsible for seeding the high initial ERES number in PVD soon after birth. To test this hypothesis, we performed time-lapse imaging using *unc-86(e1416)* mutants, in which the asymmetric cell division is disrupted. In *unc-86(e1416)* mutants, PVD and PVDsis have similar cell sizes. We found that *unc-86(e1416)* mutant PVD and PVDsis showed similar ERES numbers, which fall in between the values of WT PVD and WT PVDsis (Fig. 3b and top-right, 3c). These results are consistent with the notion that larger cells form more ERESs.

unc-86(e1416) mutants also exhibit an abnormality in PVD cell fate in addition to asymmetric division defects, both of which cause defects in ERES number. To circumvent the cell fate defect, we sought to manipulate the size of PVD with a *lin-5* mutation. LIN-5/NUMA directly regulates asymmetric cell division and cell size by specifying spindle position during cell division. It has been shown that *lin-5* mutations alter relative daughter cell size without changing anterior-posterior polarity[15]. To bypass the lethality of *lin-5* null mutants, we generated a conditional *lin-5* strain by tagging the endogenous *lin-5* locus with a zf ubiquitination sequence. We used the *unc-86* promoter to express *zif-1* to degrade zf-tagged LIN-5 in the PVD progenitor cell just before PVD birth[16]. This manipulation displaces the spindle during PVD progenitor division, resulting in several categories of cell division phenotypes that differ from animal to animal: 1) Failed cell division, 2) exaggerated asymmetry of daughter cells where the size difference between the daughter cells is larger than normal (Fig. 4b lower left), 3) reduced asymmetry of daughter cells, where the daughter cells display a less pronounced size difference (Fig. 4b lower right), and 4) WT-like asymmetry of daughter cells. We took advantage of these different phenotypes to compare initial ERES numbers in daughter cells of differing soma size at birth. We found a strong correlation between initial soma size and initial ERES number (Fig. 4c), suggesting that asymmetric cell division and cell size determine the high ERES number initiated in Phase I.

Next, we sought to address how high ERES numbers are maintained (Phase II) during PVD neurite outgrowth. MEC-3 is a transcription factor required for PVD dendrite morphogenesis and is downstream of UNC-86[17–19]. We hypothesized that *mec-3(e1338)* mutants would preserve asymmetric cell division and ERES initiation, but perturb maintenance of ERES number during PVD growth. Consistent with this hypothesis, in *mec-3(e1338)* mutants, asymmetric cell division proceeds as normal, and we observe that initial ERES number is similar to WT (Fig. 5a). However, by the L4 stage, *mec-3(e1338)* mutants showed dramatically reduced number of ERESs (Fig. 2a, b, Fig. 5a), indicating that ERES number is actively maintained in an MEC-3 dependent manner as WT PVD develops. Indeed, time course analysis of *mec-*

3(e1338) mutants show that ERES numbers in *mec-3(e1338)* are established at WT levels shortly after PVD birth, but gradually decline as the primary dendrite grows and the worm ages (Fig. 5a, b). Given the connection between soma size and initial ERES number observed in Figure 4, we wanted to test if *mec-3(e1338)* PVD soma size differs from WT. We observed that initial soma size in WT and *mec-3(e1338)* does not differ (Fig. 5b). However, by L4, *mec-3(e1338)* PVD has significantly fewer ERESs than WT as well as a significantly smaller soma size (fig. 5b), further supporting an association between ERES number and soma size. Interestingly, WT soma size appears to increase as PVD develops, while *mec-3(e1338)* soma size lacks that increase (Fig. 5b, see Discussion).

We also performed the same experiment on *unc-86(e1416)* mutants and found that *unc-86(e1416)* PVD exhibit a lower initial ERES number, and a further decline in ERES number as PVD matures (Fig. 5a, b). The more dramatic ERES phenotypes in *unc-86(e1416)* mutants may be a result of the combination of defects in asymmetric cell division and MEC-3 dependent pathways. This is consistent with the literature that UNC-86 has both an early, MEC-3 independent function and a MEC-3 dependent function at later stages[17–19] (see Discussion).

The reduction in number of ERESs, the lack of soma size increase and the defective dendrite growth of the *mec-3* mutant PVD suggest an overall lack of biosynthetic flux in these mutants. It is conceivable that MEC-3 controls a biosynthetic program to coordinately increase soma size and maintain ERES number. In the vertebrate context, the master regulator mTOR has been associated with overgrowth of neuronal soma in specific contexts[20,21]. We hypothesized that MEC-3 promotes expression or activity of *C. elegans* TOR (ceTOR) in PVD. To test this hypothesis, we first examined a transcriptional reporter of *let-363* developed by Long et al. 2002[22]. Indeed, we find that WT PVD has higher average levels of ceTOR transcriptional reporter than *mec-3*(*e1338*) PVD, while reporter levels in PDE do not change between WT and *mec-3*(*e1338*) mutant (fig. 5c). Notably, levels of the *let-363* transcriptional reporter are higher in WT PVD than its smaller cousin PDE, which also has fewer ERESs (Fig. 5c). These results imply that MEC-3 specifically upregulates ceTOR/LET-363 in PVD.

Next, we asked if *let-363* activity is required for high number of ERESs. In the constitutive *let-363(ok3018)* mutant, which exhibits an overall arrest in growth of *C. elegans*, we observe a reduction in ERES number in PVD soma (Fig. 5d). To ask if LET-363 is required cell autonomously for ERES number, we built a conditional *let-363* allele using the Cre-lox system to disrupt LET-363 specifically in PVD lineage cells (Fig. 5e, f, g). We find that when *let-363* is deleted, PVD exhibits normal initial ERES number at PVD birth but was significantly reduced by L4 (Fig. 5h). Interestingly, the conditional *let-363* mutant PVD also displayed normal soma size at PVD birth but reduced soma size by L4. Additionally, this allele showed a reduction in the size of PVD's dendritic arbor compared to WT (fig. 5e). The striking similarity between the conditional *ceTOR/let-363* phenotypes and the *mec-3*(*e1338*) phenotypes argue strongly that ceTOR is part of the MEC-3 dependent mechanisms necessary for PVD maturation.

Given the role of TOR as a nutrient sensor, we wondered whether nutrient availability has any impact on ERES number. Our hypothesis was that TOR's positive impact on ERES number requires the availability of nutrients. To test the effect of nutrient restriction on PVD ERES number, we removed worms from food just after PVD birth. The following day, starved worms displayed significantly fewer PVD ERESs than in fed worms (Fig. 6a, b). In addition, PVD somata were significantly smaller in starved vs. fed worms (Fig. 6c). In order to test whether the TOR-mediated and nutrient-mediated mechanisms on ERES act in the same genetic pathway, we starved WT and *let-363*-floxed worms. We observed that there was no significant additional reduction of PVD ERESs in the *let-363* worms upon starvation (Fig. 6d). Similarly, there was no significant difference between WT starved worms and *let-363* starved worms

(Fig. 6d). These results are consistent with the notion that the impacts of LET-363 perturbation and nutrient deprivation are due to overlapping pathways.

Next, we tested whether *mec-3(e1338)* and nutrient deprivation have independent effects on ERES number by starving *mec-3*(*e1338*) and WT worms. Once again, we observed no significant differences between *mec-3(e1338)* fed worms, *mec-3(e1338)* starved worms, and WT starved worms (Fig. 6d). However, there is a slight, though not significant, trend of especially low ERES number in worms that have both manipulations of *mec-3* perturbation and starvation, perhaps indicating that these pathways are not fully overlapping (see Discussion). Together, these findings are consistent with a model in which MEC-3 drives TOR activity (among other downstream pathways such as guidance factors), which, in the presence of nutrients, maintains high ERES number in PVD.

Interestingly, the impacts of starvation on ERES appear to be stage-specific. Nutrient deprivation of animals before PVD is born resulted in the largest reduction of ERES numbers (Fig. 6e). Nutrient deprivation of animals just after PVD birth results in a moderate reduction of ERES numbers, while nutrient deprivation of animals after PVD reaches maturity results in mild or no significant difference in ERES numbers. These results imply that ERESs are more plastic in early development and become more "static" once PVD reaches maturity. These results indicate critical periods during which ERES dynamics allow for changes in number that coincide with key developmental events (see Discussion).

In summary, we have characterized two phases of ERES dynamics contributing to high ERES number in PVD. In Phase I, UNC-86 and LIN-5 drive asymmetric cell division to generate a large PVD soma at the expense of a small and dying sister cell. The large soma likely leads to high ERES number in PVD due to cytoplasmic scaling. In Phase II, during neurite outgrowth, MEC-3, LET-363, and nutrient availability work together to actively maintain high ERES number and promote growth of the somatodendritic compartment.

Discussion:

In this study, we show that neurons with large, complex dendrites have high number of ER-exit sites in their somas. Through time-lapse imaging and mutant analyses, we addressed how the number of ER-exit sites is determined during development. Our data suggest a model in which ERES number is initially established rapidly by the size of the post-mitotic neuron at birth, and this number is actively maintained during neurite outgrowth through the action of transcription factors and adjusted by nutrient availability before the number stabilizes as the neuron matures.

We demonstrate that, in PVD, ERES number is likely determined by cell fate pathways rather than feedback from growing neurites. Previous work has shown that extrinsic cues such as target derived neurotrophins regulate survival and neuronal morphogenesis demonstrating a feedback regulation mechanism[23,24]. We hypothesized that increasing secretory demand from a developing dendrite might upregulate ERES number. The PVD dendritic arbors are not only unusually large among worm neurons but also precisely target the space between skin and muscles. In the dendrite guidance factor and receptor mutants, the dendritic arbor is drastically smaller and fails to grow into the skin-muscle junctions[11–13]. However, we found these mutants did not show abnormalities in the number of early secretory organelles in PVD. These results argue strongly that the size, shape and precise targeting of PVD dendrites are dispensable for the determination of their ERES number. Consistent with this notion, we demonstrate that GFP::SEC-16 puncta emerge rapidly during PVD birth, and establish high ERES numbers before neurite

outgrowth. These findings suggest a cell fate model, in which secretory organelle number is encoded into a neuron's identity.

What aspects of the neuron's identity determines ERES number? We explored this question with a two-pronged approach. First, we asked whether ERES numbers scale with cell size. Our direct imaging experiments suggest that PVD inherits a large soma due to the asymmetric cell division. We used different ways to manipulate the size of PVD and found that there is a strong correlation between cell size and ERES number. Second, we identified transcription factors that regulate ERES numbers in PVD. Both UNC-86 and MEC-3 are required for the normal level of ERES in PVD. Closer examination of *unc-86(e1416)* and *mec-3(e1338)* phenotypes led to the notion that three distinct phases exist in the establishment and maintenance of ERES in PVD.

The first phase utilizes asymmetric cell division to generate a large PVD soma. This phase is a rapid process because ERESs emerge as mitosis concludes. This process requires both UNC-86 and regulators of cell division plane including LIN-5/NUMA. In the second phase, both MEC-3, UNC-86 and sufficient nutrients are needed to actively maintain ERES number. In *mec-3(e1338)* or *unc-86(e1416)* mutants, as well as starvation conditions, the number of ERESs decreases in this phase. In the third phase, ERES numbers become stable because late starvation does not lead to a similar reduction of ERES number as early starvation.

The differences in ERES number phenotypes between *unc-86(e1416)* and *mec-3(e1338)* are consistent with their differential expression. In *unc-86(e1416)* mutants, both the establishment and the maintenance of ERES number are defective, while MEC-3 is only required for the maintenance of ERES number. It was shown that UNC-86 expression turns on in the PVDmother and is required for asymmetric cell division[16]. UNC-86 is also required for the subsequent activation of MEC-3[17–19]. Thus, MEC-3 is expressed later, and then forms a heterodimer with UNC-86 to activate lineage specific transcriptional programs[17–19,25].

TOR's function and signaling pathways in growth and nutrient sensing has been intensively studied in various contexts, but its role in normal physiological growth of neurons *in vivo* is not well understood. Kwon *et al.* [20] observed no impact of TOR inhibition on physiological soma size of granule cells. However, they did find that abnormal soma expansion of PTEN-deficient mice was dependent on TOR. Choi *et al*. found that rapamycin-mediated inhibition of TOR in cultured embryonic rat hippocampal neurons impaired axon growth but not dendrite growth[26]. We report a cell-specific requirement for *ceTOR/let-363* in the normal physiological growth of PVD. *ceTOR/let-363*'s role in PVD appears to coordinate soma size, ERES number, and dendrite size, suggesting it may be a cell-intrinsic master regulator for overall biosynthesis and cell size in PVD. The impact on soma size differs from the finding by Kwon *et al*. that TOR disruption did not impact WT soma size in murine granule cells[20]. Several factors may account for the apparent discrepancy in these results. Granule cells are among the smallest cells in vertebrate brains[27] and their physiological growth may therefore be less sensitive to TOR. More broadly, TOR growth dependence may vary between neuron types and species. Further research is required to test whether differential TOR activity is a general feature of neuron size regulation.

There are several potential models for why ERES number decreases in starvation and in TOR mutants. TOR plays well-established roles in promoting protein translation and lipid biosynthesis, while inhibiting autophagy[28–31]. It is possible that reduction in protein translation and resultant reduction of secretory flux reduces ERES number[32]. In addition, a lack of TOR-mediated lipid synthesis may inhibit growth of the soma and ER membrane, limiting ERES emergence (as discussed above). Another possibility is that starvation and lack of TOR activity disinhibits autophagy of ERES directly, or disinhibits ER-phagy, as

seen in yeast and *Drosophila*[33,34], which would result in a reduced ER area that could promote ERES fusion.
Our direct observation of SEC-16 dynamics and nutrient deprivation experiments also revealed that ERES structure might change their physical properties and biochemical composition as the structure matures. An emerging body of evidence indicates that liquid-liquid phase separation (LLPS) may play an important role in ERES formation and maintenance. Previous work suggests that ERESs are dynamic, self-organizing structures[35–38]. In addition, mammalian SEC-16 exhibits liquid-liquid phase separation (LLPS) behavior *in vitro* and *in vivo*, forming condensates that recruit COPII components and other early secretory pathway proteins[39]. Disruption of SEC-16 LLPS activity impairs secretory pathway structure and function in mammalian cells[39].

Our observations of ERES establishment in PVD are consistent with several properties of LLPS. The dependence of initial ERES number on PVD cell size is consistent with the inherent size scaling behavior of LLPS condensates[40]. Asymmetric cell division of PVDmother may therefore provide sufficient cytoplasmic volume and ER membrane to nucleate the number of GFP::SEC-16 LLPS droplets required to establish PVD's high ERES number. Quantitative computational models that describe ERES as self-organizing LLPS-like clusters[35,36,38] predict that smaller cells will have reduced numbers of ERESs, consistent with our observations of fewer PVD ERESs in mutants such as *ceTOR/let-363* that have smaller somas. Additional studies will be required to confirm or disprove the role of LLPS in the establishment and maintenance of ERES number in neurons *in vivo*[41].

These results raise many new questions regarding the molecular mechanisms of ERES maturation and stability in the context of neuronal development and maintenance. Since ERESs form an essential component of secretory pathways affecting most transmembrane and secreted proteins, regulation of ERESs in neurons are likely to be critical for many functions of the nervous system.

Methods

C. elegans Strains

All strains were grown on nematode growth medium (NGM) plates seeded with OP50 *E. coli* at 20°C unless otherwise stated for experimental conditions. N2 Bristol was used as wild-type strain. Mutant alleles and transgenes used in this study are listed in Table S1. Lin-5 mutants were kindly provided by Dr. Xing Liang.

Plasmids

Plasmid constructs for *C. elegans* expression (Table S1) were generated in pSM delta vector as a backbone, which was kindly provided by Dr. Andrew Fire. FLP,PVD>mScarlet, Pmec-17::mScarlet(KE51) & plin-32::FLP constructs were kindly provided by Dr. Chris Tzeng and Dr. Kelsie Eichel. DNA constructs were then assembled into plasmid constructs using Gibson cloning methods.

C. elegans transformation

Transgenic extrachromosomal arrays were generated using a standard microinjection protocol[42]. In short, plasmid constructs and co-injection marker were mixed and injected to distal arm of the gonad of young adult animals. F1 animals were then screened for transgenic lines. The details of transgenic arrays can be found on Table S1.

CRISPR Genome editing

CRISPR knock-ins were generated by direct gonadal injection of Cas9 protein (IDT) duplexed with tracrRNA and targeting crRNA (IDT) along with respective repair templates[43].
For long insertions (> 150bp), knock-in templates (GFP-FLPon-SEC-16A.2) were PCR amplified from pSK–FLPon–GFP vectors[44] with ultramer oligonucleotides (Integrated DNA Technologies) containing 100 bp of flanking genome homology. PCR products were purified by ethanol precipitation or PCR cleanup and used for injection at 300ng/µl concentrations. For short insertions (loxp sites), synthetic single-stranded DNA oligos (IDT Ultramers) were used as templates and injected at 600nM concentrations. F1 animals were screened by PCR genotyping. Heterozygous F1 animals were homozygoused and the insertions were verified by Sanger sequencing. The following guide RNA sequences were used for genome edits: GFP-FLPon-SEC-16A.2: TGTTGCCAATAGAAGCTCAT; *let-363*-loxp: tttttctatattcgaaccaa & tgatattttgaaatatgcaa.

***C. elegans* synchronization, staging and nutrient deprivation**

Gravid adults were washed off from eight to ten 6cm-plates with M9 buffer. Animals were then bleached in hypochlorite solution to obtain embryos. Embryos were washed with M9 buffer two to three times and then resuspended in M9 and allowed to hatch overnight into L1-arrested animals. L1-arrest animals were kept for maximum of 24hr before plating onto OP50-seeded NGM plates.

For the nutrient deprivation protocol, arrested L1s were plated onto freshly seeded OP50 NGM plates, with varying amounts of OP50 in order to vary developmental stage of starvation. Animals were then monitored over the next 20-30 hr, and at the appropriate stage (either several hours before PVD-birth or immediately following PVD-birth) worms were either allowed to continue growing on starved plates or removed from OP50 onto either nutrient-free NGM plates (for starvation), or OP50-seeded NGM plates (fed controls). Data from fed and starved worms was collected the following day.

For time course experiments, animals were synchronized as described above and examined under a Zeiss Axioplan fluorescence scope with 63X Plan-Apochromat 63 × /1.4 NA objective for counting of ERES at indicated timepoints.

To image early PVD morphogenesis events (L2 animals), L1-arrest animals were grown on OP50-seeded NGM plates for 25-28 hr depending on the strain at ~20°C to reach L2 stage. After L2 stage has been reached, animals were monitored every 30 minutes under Zeiss Axioplan fluorescene scope with 63X Plan-Apochromat 63 × /1.4 NA objective. Animals were mounted on slides for imaging when majority of animals reached desired developmental stage (PVD precursor stage). To image mature PVDs and PDEs and TRNs, L4 animals, identified based on vulval development, were mounted on slides.

Microscopy

For still confocal images, hermaphrodite worms at L2 or L4 stage worms were immobilized on 2-3% agarose pads using 10mM levamisole in M9 buffer. Images were obtained on a spinning disk system (3i) with a CSU-W1 spinning disk (Yokogawa), 405-nm, 488-nm and 561-nm solid-state lasers, a C-Apochromat 63×/1.2 NA water-immersion objective, and a Prime95B camera (Photometrics). Z stacks with 0.25-0.5 µm sections spanning the imaged neurons were taken. For live-imaging of developing worms, L2 stage hermaphrodite worms were immobilized on 7.5% agarose pads using 2.5mM levamisole in M9 buffer. Slides were sealed with VALAP to prevent agarose pad from desiccation. FRAP of ERES was performed on the same system with a Vector diffraction-limited xy scanner (3i). Live-imaging was performed with the same system. Z stacks with 0.4 µm sections were obtained every 3 minutes for maximum duration of 6 hours.

Image Analysis

ERES were counted manually from unmodified z-stacked images, using the neuron plasma membrane marker mCherry::PH(PLCγ), or cytoplasmic mScarlet to identify cells of interest (COI), and counting the number of endogenous GFP::SEC-16A.2 puncta in COI somas. Two puncta that appeared to be in contact but had clearly separate centers of highest intensity were defined as doublets and counted as two ERESs. Counting criteria were the same for counts made in z-stack images taken on the 3i spinning disk confocal and counts made on animals directly under the Zeiss Axioplan microscope under the same magnification. For fluorescence intensity quantifications of nuclear-localized Plet-363::GFP, total fluorescence intensity values were obtained at ROIs of SUM-projected Z-stacks using ImageJ.

Electron microscopy

Wild-type N2 worms were prepared for conventional EM by high pressure freezing/freeze-substitution. Worms in M9 containing 20% BSA and *E. coli* were frozen in 100 mm well specimen carriers (Type A) opposite a hexadecane coated flat carrier (Type B) using a BalTec HPM 01 high-pressure freezer (BalTec, Lichtenstein). Freeze-substitution in 1% OsO_4, 0.1% uranyl acetate, 1% methanol in acetone, containing 3% water[45,46] was carried out with a Leica AFS2 unit. Following substitution, samples were rinsed in acetone, infiltrated and then polymerized in Eponate 12 resin (Ted Pella, Inc, Redding, CA). Serial 50 nm sections were cut with a Leica UCT ultramicrotome using a Diatome diamond knife, picked up on Pioloform coated slot grids and stained with uranyl acetate and Sato's lead[47]. Sections were imaged with an FEI Tecnai T12 TEM at 120 kV using a Gatan 4k x 4 k camera. TrakEM2 in Fiji was used to align serial sections [48–50]. Modeling of serial sections was performed with IMOD[51].

Neuron Soma Measurements:

Z-stack still images taken on the 3i spinning disc microscope, as described, above were projected into a single plane using ImageJ software. ROI's were drawn around the projected soma, and the area of this ROI was measured in um as an estimation of the maximal cross-section of the cell in the xy plane.

Quantification of dendritic arbor

Images were straightened with the ImageJ software (US National Institutes of Health) using the primary dendrite as a reference. In L4 animals, a 100micron long rectangular ROI was placed starting at the center of PVD soma extending 100 microns anteriorly, containing the entire width of the animal. The number of secondary, tertiary and quaternary branches within this ROI was counted. Any protrusion from the primary dendrite was classified as a secondary branch, and any correctly-oriented protrusion from the tertiary dendrite was classified as a quaternary branch.

Quantification and statistical analysis

All statistical analysis was done using GraphPad Prism software. All statistical parameters can be found in the corresponding figure legends. No statistical methods were used to predetermine the sample size.

Acknowledgements

We thank C. Wicky and F. Muller for strain FR297[22]; X. Liang for *lin-5* reagents; C. Tzeng for expression constructs; J. Lee for assistance with long-term time-lapse imaging; L. Tao for guidance receptor mutant morphology images; C. Richardson and members of the Shen Lab for conversation and reagents.

References

1. Ye, B. *et al. Growing dendrites and axons differ in their reliance on the secretory pathway*.

2. Gorelick, F. S. & Jamieson, J. D. Structure–function Relationships in the Pancreatic Acinar Cell. *Physiol. Gastrointest. Tract, Two Vol. Set* 1341–1360 (2012) doi:10.1016/B978-0-12-382026-6.00049-X.

3. Griffiths, G., Pfeiffer, S., Simons, K. & Matlin, K. Exit of newly synthesized membrane proteins from the trans cisterna of the Golgi complex to the plasma membrane. *J. Cell Biol.* **101**, 949–964 (1985).

4. Clermont, Y., Xia, L., Rambourg, A., Turner, J. D. & Hermo, L. Structure of the Golgi apparatus in stimulated and nonstimulated acinar cells of mammary glands of the rat. *Anat. Rec.* **237**, 308–317 (1993).

5. Farhan, H., Weiss, M., Tani, K., Kaufman, R. J. & Hauri, H. P. Adaptation of endoplasmic reticulum exit sites to acute and chronic increases in cargo load. *EMBO J.* **27**, 2043–2054 (2008).

6. Barlowe, C. & Helenius, A. Cargo Capture and Bulk Flow in the Early Secretory Pathway. *Annu. Rev. Cell Dev. Biol.* **32**, 197–222 (2016).

7. Peotter, J., Kasberg, W., Pustova, I. & Audhya, A. COPII-mediated trafficking at the ER/ERGIC interface. *Traffic* vol. 20 491–503 (2019).

8. Witte, K. *et al.* TFG-1 function in protein secretion and oncogenesis. *Nat. Cell Biol.* **13**,

550–8 (2011).

9. Nakano, A. & Muramatsu, M. A novel GTP-binding protein, Sar1p, is involved in transport from the endoplasmic reticulum to the Golgi apparatus. *J. Cell Biol.* **109**, 2677–2691 (1989).

10. Long, K. R. *et al.* Sar1 assembly regulates membrane constriction and ER export. *J. Cell Biol.* **190**, 115–128 (2010).

11. Liu, O. W. & Shen, K. The transmembrane LRR protein DMA-1 promotes dendrite branching and growth in C. elegans. *Nat. Neurosci. 2011 151* **15**, 57–63 (2011).

12. Dong, X. *et al.* Precise regulation of the guidance receptor DMA-1 by KPC-1/Furin instructs dendritic branching decisions. *Elife* **5**, (2016).

13. Zou, W. *et al.* A Dendritic Guidance Receptor Complex Brings Together Distinct Actin Regulators to Drive Efficient F-Actin Assembly and Branching. *Dev. Cell* **45**, 362-375.e3 (2018).

14. Teuliere, J., Kovacevic, I., Bao, Z. & Garriga, G. The Caenorhabditis elegans gene ham-1 regulates daughter cell size asymmetry primarily in divisions that produce a small anterior daughter cell. (2018) doi:10.1371/journal.pone.0195855.

15. Jankele, R., Jelier, R. & Gönczy, P. Physically asymmetric division of the c. Elegans zygote ensures invariably successful embryogenesis. *Elife* **10**, 1–66 (2021).

16. Finney, M. & Ruvkun, G. The unc-86 gene product couples cell lineage and cell identity in C. elegans. *Cell* **63**, 895–905 (1990).

17. Chalfie, M. & Au, M. Genetic control of differentiation of the Caenorhabditis elegans touch receptor neurons. *Science* **243**, 1027–1033 (1989).

18. Xue, D., Tu, Y. & Chalfie, M. Cooperative interactions between the Caenorhabditis elegans homeoproteins UNC-86 and MEC-3. *Science* **261**, 1324–1328 (1993).

19. Xue, D., Finney, M., Ruvkun, G. & Chalfie, M. Regulation of the mec-3 gene by the C.elegans homeoproteins UNC-86 and MEC-3. *EMBO J.* **11**, 4969–4979 (1992).

20. Kwon, C. H., Zhu, X., Zhang, J. & Baker, S. J. mTor is required for hypertrophy of Pten-deficient neuronal soma in vivo. *Proc. Natl. Acad. Sci. U. S. A.* **100**, 12923–12928 (2003).

21. Kwon, C. H. *et al.* Pten regulates neuronal soma size: A mouse model of Lhermitte-Duclos disease. *Nat. Genet.* **29**, 404–411 (2001).

22. Long, X. *et al.* TOR deficiency in C. elegans causes developmental arrest and intestinal atrophy by inhibition of mRNA translation. *Curr. Biol.* **12**, 1448–1461 (2002).

23. Fawcettt, J. W. & Keynes, R. J. Peripheral Nerve Regeneration. *https://doi-org.laneproxy.stanford.edu/10.1146/annurev.ne.13.030190.000355* **13**, 43–60 (2003).

24. Purves, D., Snider, W. D. & Voyvodic, J. T. Trophic regulation of nerve cell morphology and innervation in the autonomic nervous system. *Nat. 1988 3366195* **336**, 123–128 (1988).

25. Duggan, A., Ma, C. & Chalfie, M. Regulation of touch receptor differentiation by the Caenorhabditis elegans mec-3 and unc-86 genes. *Development* **125**, 4107–4119 (1998).

26. Choi, Y.-J. *et al.* Tuberous sclerosis complex proteins control axon formation. (2008) doi:10.1101/gad.1685008.

27. D'Angelo, E. Granule cells and parallel fibers. *Essentials Cerebellum Cerebellar Disord. A Prim. Grad. Students* 177–182 (2016) doi:10.1007/978-3-319-24551-5_20/FIGURES/1.

28. Keith Blackwell, T., Sewell, A. K., Wu, Z. & Han, M. TOR Signaling in Caenorhabditis elegans Development, Metabolism, and Aging. *Genetics* **213**, 329 (2019).

29. Nandagopal, N. & Roux, P. P. Regulation of global and specific mRNA translation by the mTOR signaling pathway. *Translation* **3**, e983402 (2015).

30. Laplante, M. & Sabatini, D. M. An Emerging Role of mTOR in Lipid Biosynthesis. *Curr. Biol.* **19**, R1046–R1052 (2009).

31. Deleyto-Seldas, N. & Efeyan, A. The mTOR–Autophagy Axis and the Control of Metabolism. *Front. Cell Dev. Biol.* **9**, 1519 (2021).

32. Zacharogianni, M. *et al.* ERK7 is a negative regulator of protein secretion in response to amino-acid starvation by modulating Sec16 membrane association. *EMBO J.* **30**, 3684–3700 (2011).

33. Hamasaki, M., Noda, T., Baba, M. & Ohsumi, Y. Starvation Triggers the Delivery of the Endoplasmic Reticulum to the Vacuole via Autophagy in Yeast. doi:10.1111/j.1600-0854.2004.00245.x.

34. Zhao, X. *et al.* Sec22 regulates endoplasmic reticulum morphology but not autophagy and is required for eye development in Drosophila. *J. Biol. Chem.* **290**, 7943–7951 (2015).

35. Heinzer, S., Wörz, S., Kalla, C., Rohr, K. & Weiss, M. A model for the self-organization of exit sites in the endoplasmic reticulum. *J. Cell Sci.* **121**, 55–64 (2008).

36. Farhan, H., Weiss, M., Tani, K., Kaufman, R. J. & Hauri, H. P. Adaptation of endoplasmic reticulum exit sites to acute and chronic increases in cargo load. *EMBO J.* **27**, 2043–2054 (2008).

37. Tillmann, K. D. *et al.* Regulation of Sec16 levels and dynamics links proliferation and secretion. *J. Cell Sci.* **128**, 670–682 (2015).

38. Speckner, K., Stadler, L. & Weiss, M. Unscrambling exit site patterns on the endoplasmic reticulum as a quenched demixing process. *Biophys. J.* **120**, 2532–2542 (2021).

39. Gallo, R., Rai, A. & Pelkmans, L. DYRK3-Controlled Phase Separation Organizes the Early Secretory Pathway. *bioRxiv* 2020.02.10.941757 (2020) doi:10.1101/2020.02.10.941757.

40. Brangwynne, C. P. Phase transitions and size scaling of membrane-less organelles. *J. Cell Biol.* **203**, 875–881 (2013).

41. Alberti, S., Gladfelter, A. & Mittag, T. Considerations and Challenges in Studying Liquid-

Liquid Phase Separation and Biomolecular Condensates. *Cell* **176**, 419–434 (2019).

42. Mello, C. & Fire, A. Chapter 19 DNA Transformation. *Methods Cell Biol.* **48**, 451–482 (1995).

43. Paix, A., Folkmann, A. & Seydoux, G. Precision genome editing using CRISPR-Cas9 and linear repair templates in C. elegans. *Methods* **121**–**122**, 86–93 (2017).

44. McDonald, N. A., Fetter, R. D. & Shen, K. Assembly of synaptic active zones requires phase separation of scaffold molecules. *Nat. 2020 5887838* **588**, 454–458 (2020).

45. Buser, C. & Walther, P. Freeze-substitution: The addition of water to polar solvents enhances the retention of structure and acts at temperatures around -60°C. *J. Microsc.* **230**, 268–277 (2008).

46. Walther, P. & Ziegler, A. Freeze substitution of high-pressure frozen samples: the visibility of biological membranes is improved when the substitution medium contains water. *J. Microsc.* **208**, 3–10 (2002).

47. Sato, T. A modified method for lead staining of thin sections. *J. Electron Microsc. (Tokyo).* **17**, 158–159 (1968).

48. Saalfeld, S., Fetter, R., Cardona, A. & Tomancak, P. Elastic volume reconstruction from series of ultra-thin microscopy sections. *Nat. Methods 2012 97* **9**, 717–720 (2012).

49. Cardona, A. *et al.* TrakEM2 Software for Neural Circuit Reconstruction. *PLoS One* **7**, e38011 (2012).

50. Schindelin, J. *et al.* Fiji: an open-source platform for biological-image analysis. *Nat. Methods 2012 97* **9**, 676–682 (2012).

51. Kremer, J. R., Mastronarde, D. N. & McIntosh, J. R. Computer visualization of three-dimensional image data using IMOD. *J. Struct. Biol.* **116**, 71–76 (1996).

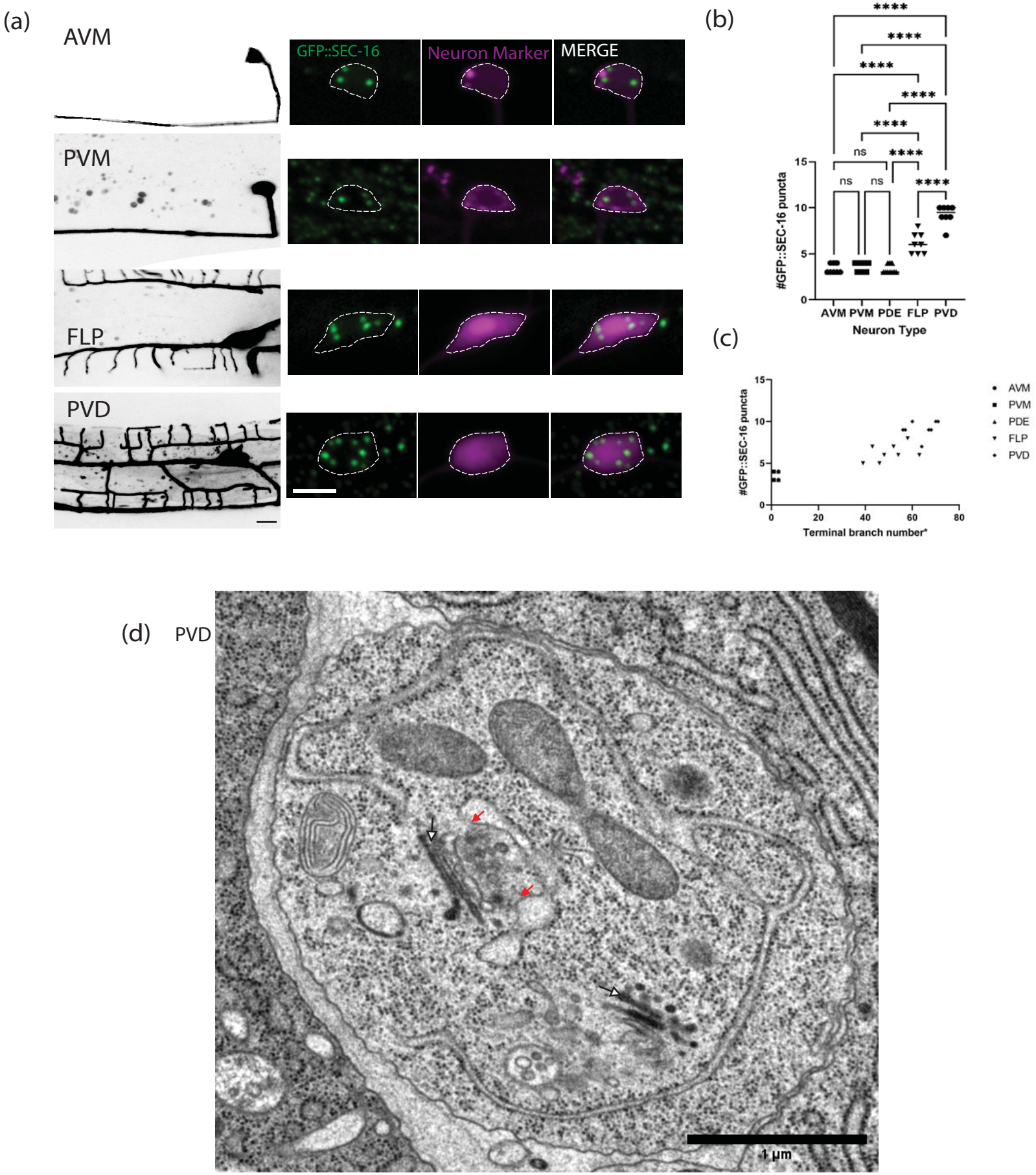
(a)
AVM
PVM
FLP
PVD
GFP::SEC-16
Neuron Marker
MERGE
(b)
****
ns
#GFP::SEC-16 puncta
AVM PVM PDE FLP PVD
Neuron Type
(c)
#GFP::SEC-16 puncta
Terminal branch number*
AVM
PVM
PDE
FLP
PVD
(d)
PVD
1 µm

(e)

PVD

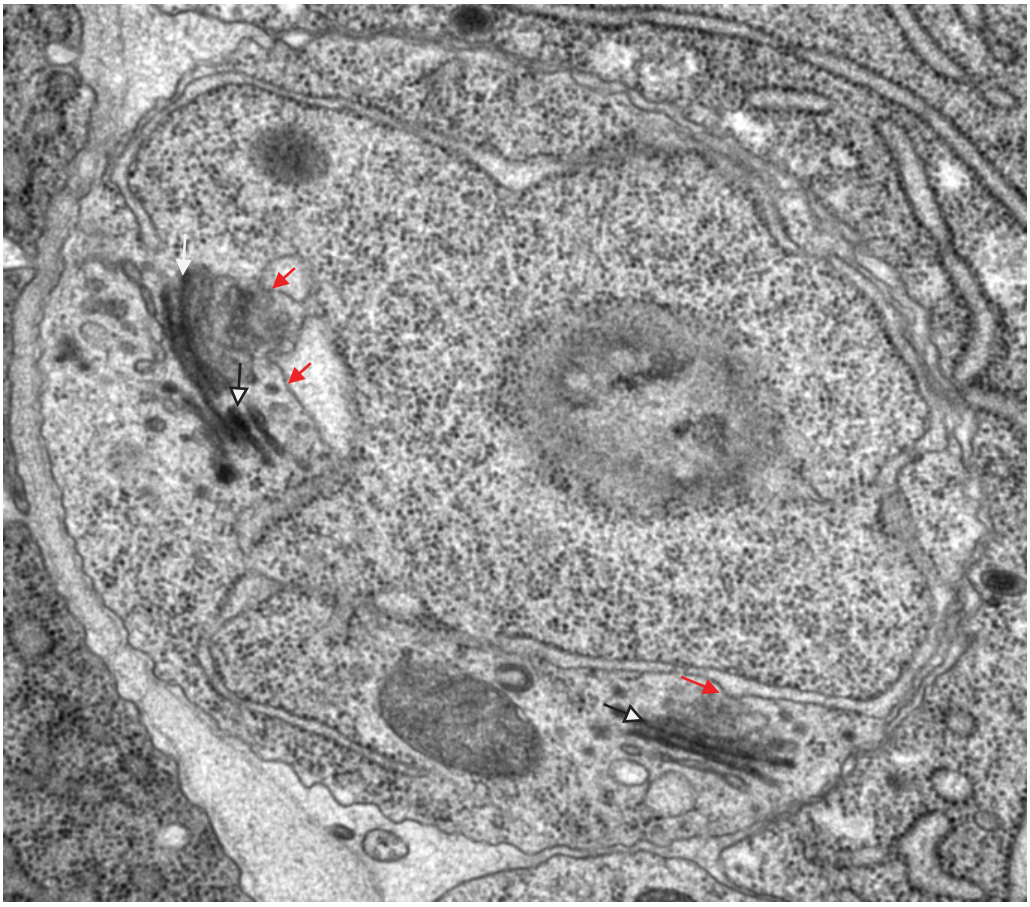

(f)

PDE

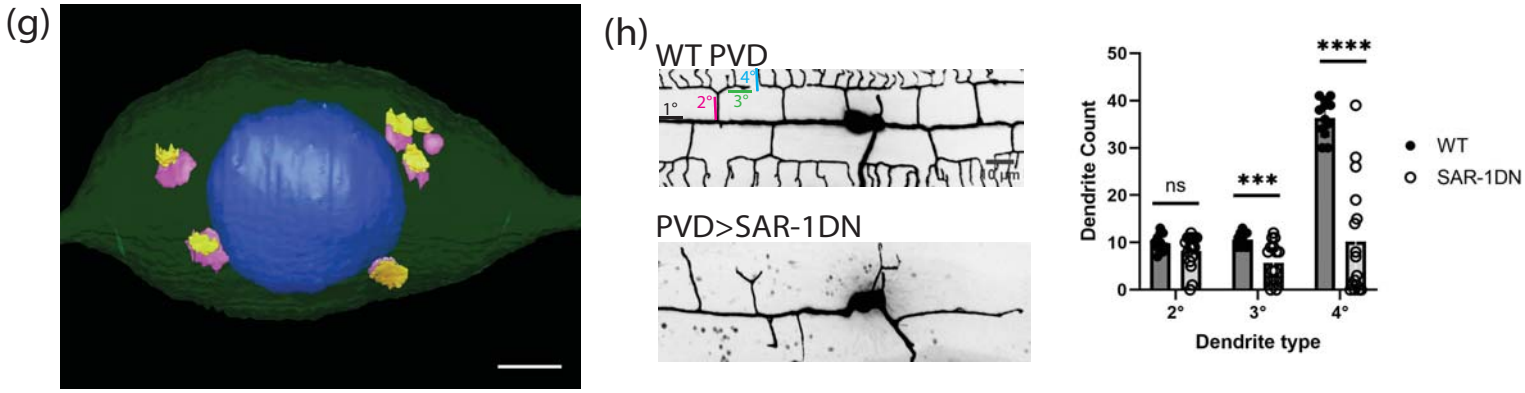

Fig.1: Larger neurons have more ER-exit sites (ERESs) in their somas. (a) Confocal fluorescence microscopic images of neuron morphology on the left (scale bar = 10µm), with closeups of soma and an endogenous ERES marker, GFP::SEC-16, on the right (scale bar = 5µm). (b) Quantification of number of GFP::SEC-16 puncta per soma in different cell types. Significance determined by one-way ANOVA, ****p<.0001. Electron microscopic (EM) images of PVD (d, e) and PDE (f) soma. Red arrows indicate ER-exit sites (ERES). Black & white arrows indicate Golgi stacks. (g) 3-D model of PVD soma constructed from EM images showing nucleus in blue, with cis (purple) and trans (yellow) cisternae of Golgi. Scale bar =1µm. (h) Representative images of WT PVD and PVD with exogenously expressed SAR-1 dominant negative (SAR-1DN), with quantifications of secondary (2°), tertiary (3°) and quaternary (4°) dendrites in WT (n=12 animals) and SAR-1-DN (n=16 animals). Significance determined by multiple t tests, ***p<.001, ****p<.0001.

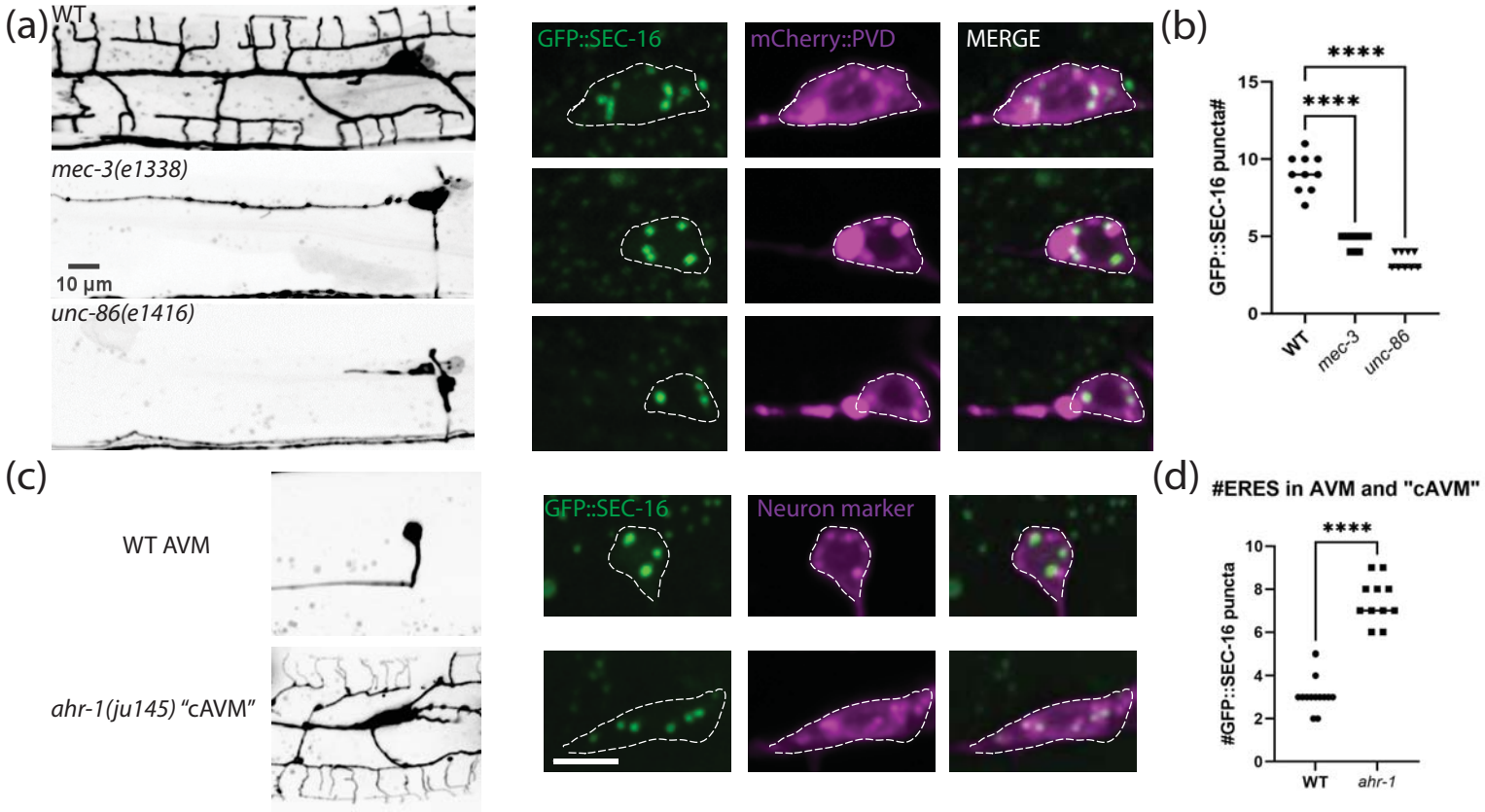

Fig.2: Cell fate mutants that alter neuron size perturb ERES abundance. (a & c) confocal fluorescence microscopy of neuron morphology of wildtype (WT) and mutant worms on the left (scale bars = 10µm, with closeups of soma and an endogenous ERES marker, GFP::SEC-16, on the right (scale bar = 5µm). (b & d) Quantification of number of GFP::SEC-16 puncta per soma. Significance determined by one-way ANOVA in (b), and Welch's t-test in (d), ****p<.0001.

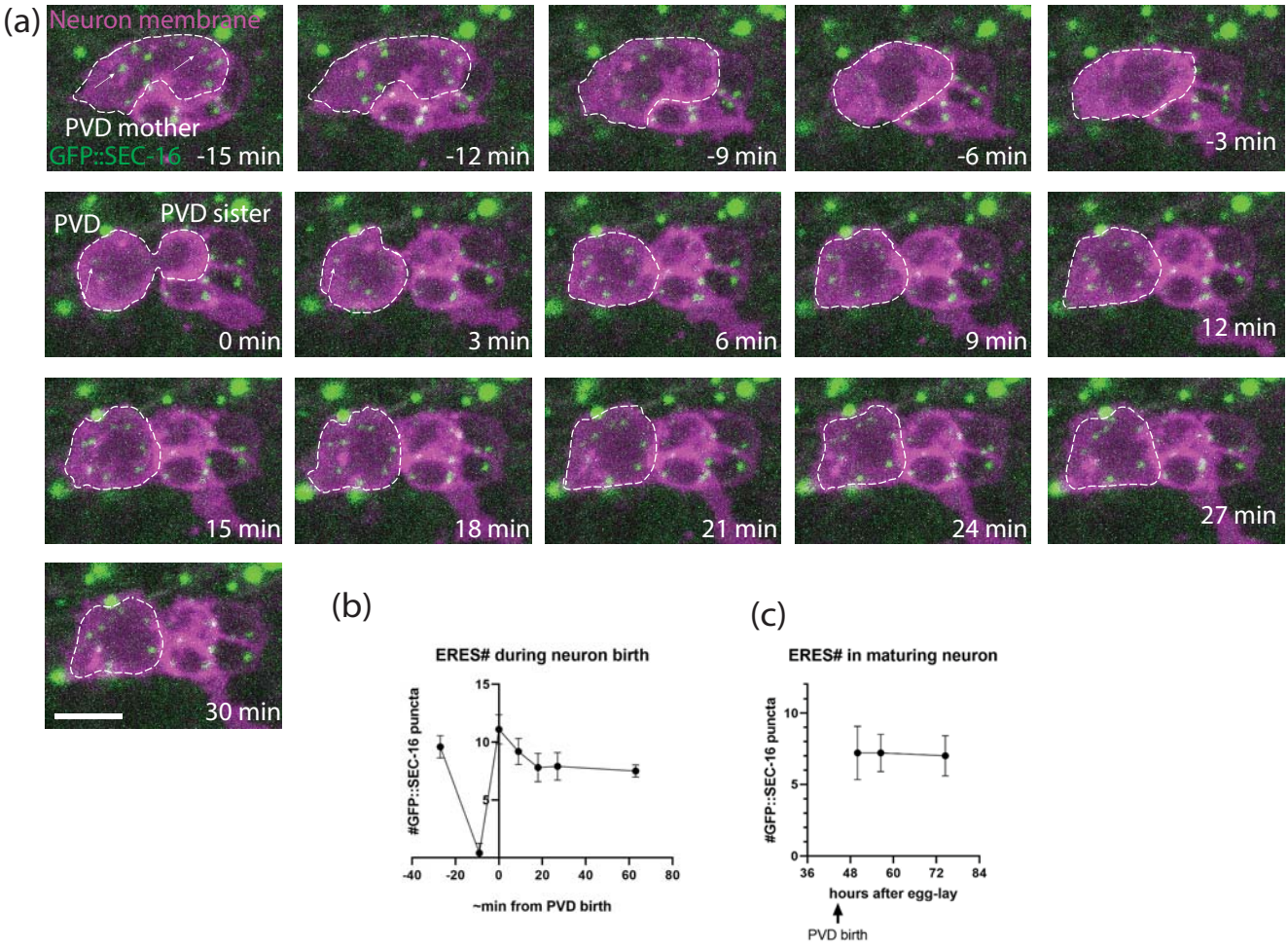

Fig. 3: ERES number is established rapidly (Phase 1) after neuron birth and persists over time. (a) Timelapse confocal fluorescence microscopic images of PVD cell birth in wildtype L2 worms with Plin-32::mCherry labeling neuron membranes and an endogenous fusion protein GFP::SEC-16 labeling ERESs (scale bar = 5µm). (b) Quantification of ERES number from longterm timelapse imaging during PVD birth. (c) Quantification of ERES number after PVD birth, via confocal microscopy, as worm matures.

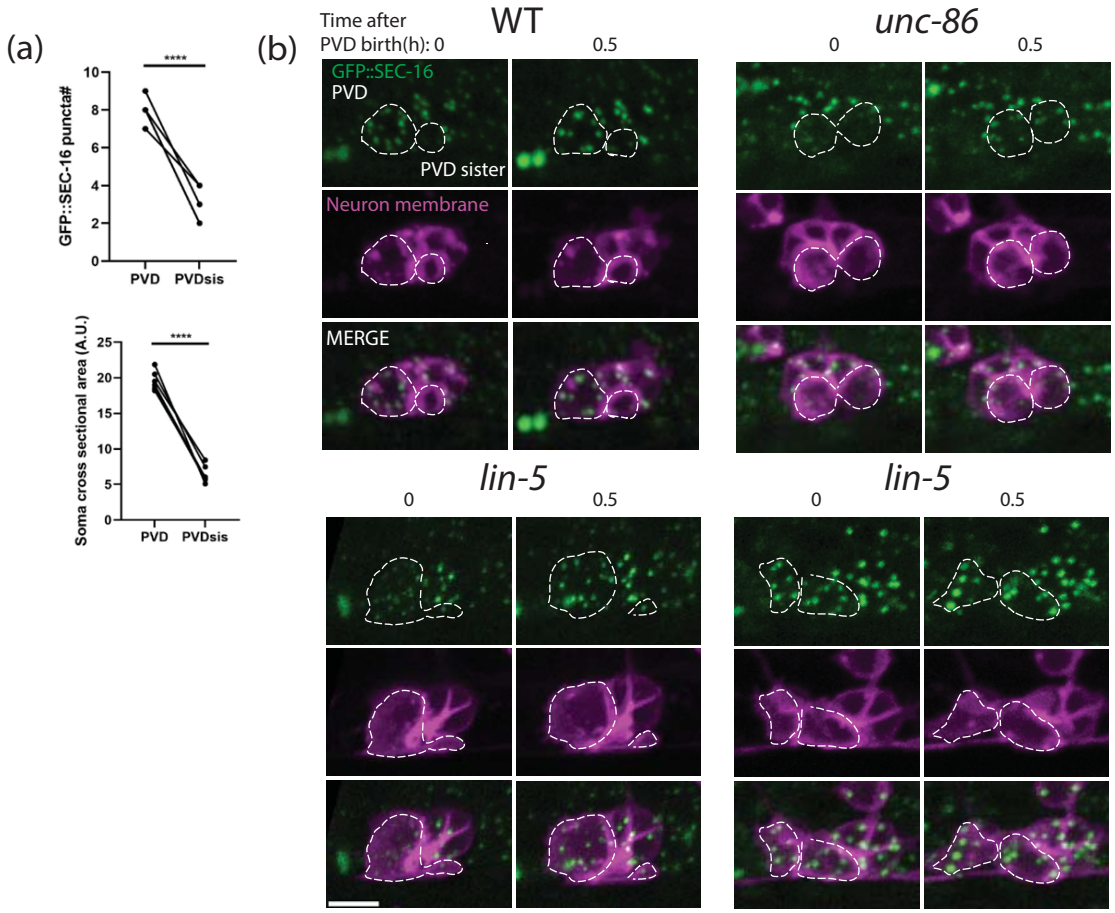

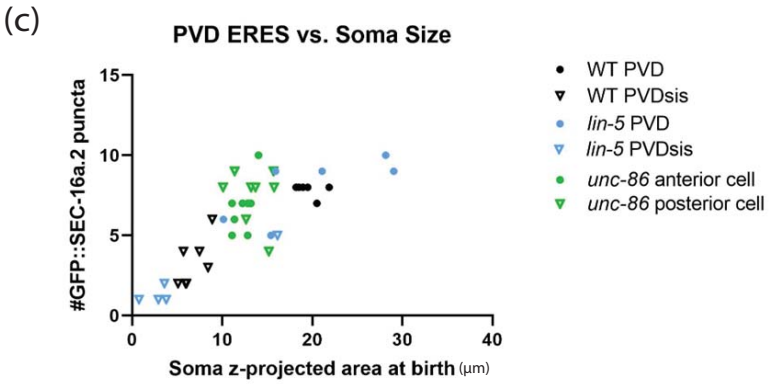

Pearson r	
r	0.7942
95% confidence interval	0.6413 to 0.8864
R squared	0.6307
P value	
P (two-tailed)	<0.0001
P value summary	****
Significant? (alpha = 0.05)	Yes

Fig. 4: Asymmetric cell division is important for initiation (Phase 1) of ERES number. (a) Quantification of ERES number shortly after birth (top), and soma cross-sectional area at birth (bottom) in PVD and PVDsister. (b) Representative images of wildtype (WT) and mutant worms at PVD birth and 0.5 hour after birth. *lin-5* mutants sometimes increase asymmetry of division (bottom left) and sometimes reduce asymmetry of division (bottom right). Scale bar = 5µm. (c) Quantification (left) and significance of correlation (right) of ERES number and cross-sectional soma area in WT and mutants.

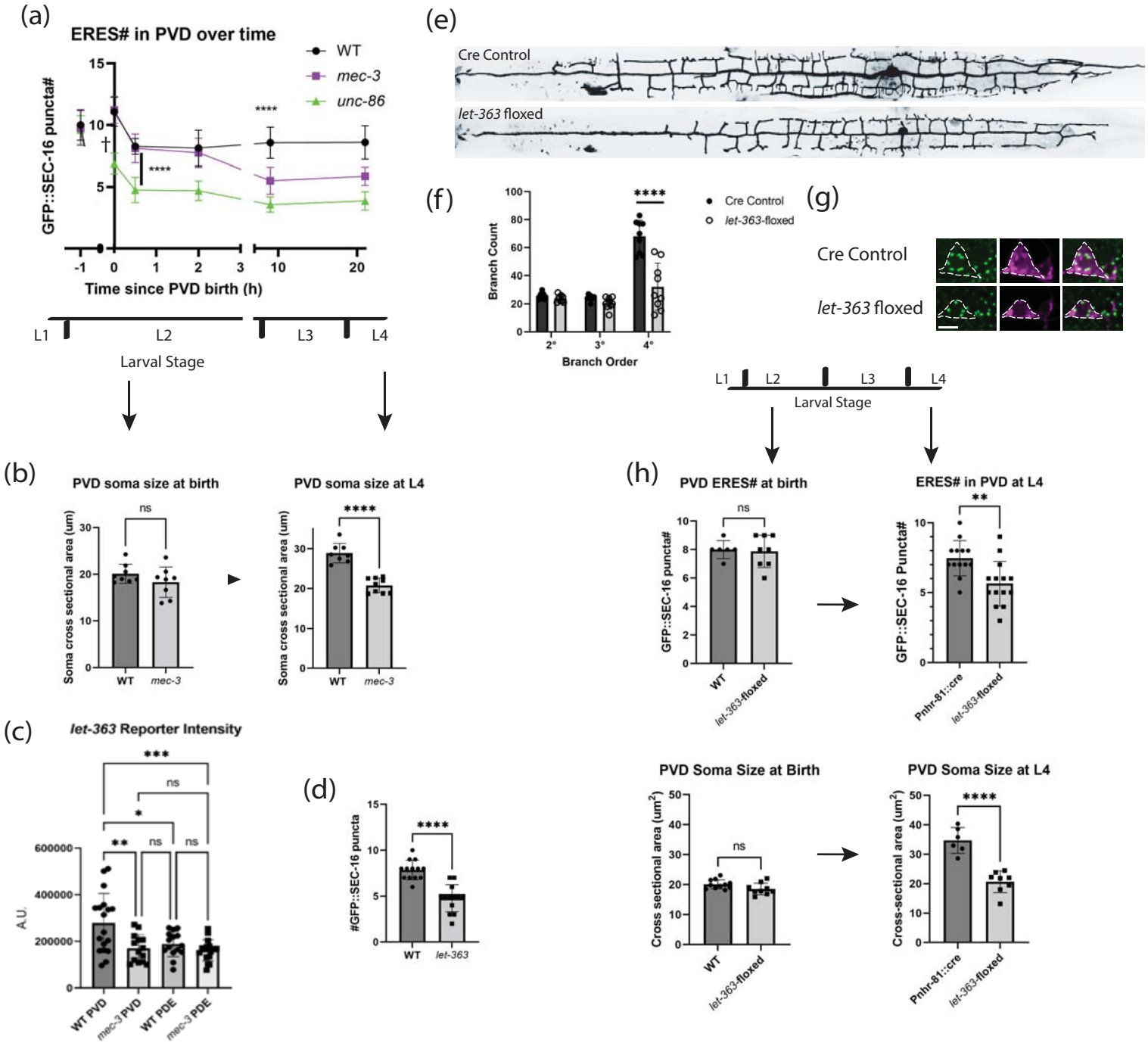

Fig. 5: MEC-3 and LET-363 maintain ERESs during neurite outgrowth in PVD. (a) Time course of ERES number in wildtype (WT) and cell fate mutants. †Points at t=0 (PVD birth) were counted from time-lapse images to provide accurate timing information. Significance determined by one-way ANOVA, ****p<.0001. (b) Soma cross-sectional area of WT and *mec-3* PVD at birth (left) and larval stage 4 (right). (c) Plet-363::GFP ceTOR transcriptional reporter intensity in PVD and PDE in WT and *mec-3* animals at larval stage 3. Significance determined by one-way ANOVA, *p<.05,**p<.01,***p<.001. (d) Quantification of number of GFP::SEC-16 puncta in wildtype vs. ce*TOR/let-363(ok3018)* constitutive mutant animal PVD somas. (e) Confocal fluorescence microscopic images of PVD morphology in control and mutant worms, with (f) quantification of branches. Significance determined by unpaired Student's t test ****p<.0001 (g) Confocal fluorescence microscopic images of PVD soma and endogenous ERES marker, GFP::SEC-16 in Pnhr-81::cre control worms (top) and conditionally floxed *let-363* worms (bottom). Scale bar = 5µm. (h) Quantification of number of GFP::SEC-16 puncta (top) and soma cross-sectional area (bottom) per PVD soma in control and mutant L2 (left) and L4 (right) worms. Significance determined by unpaired Student's t test, **p<.01, ****p<.0001. Larval stages from youngest to oldest: L1, L2, L3, L4. YA = Young Adult.

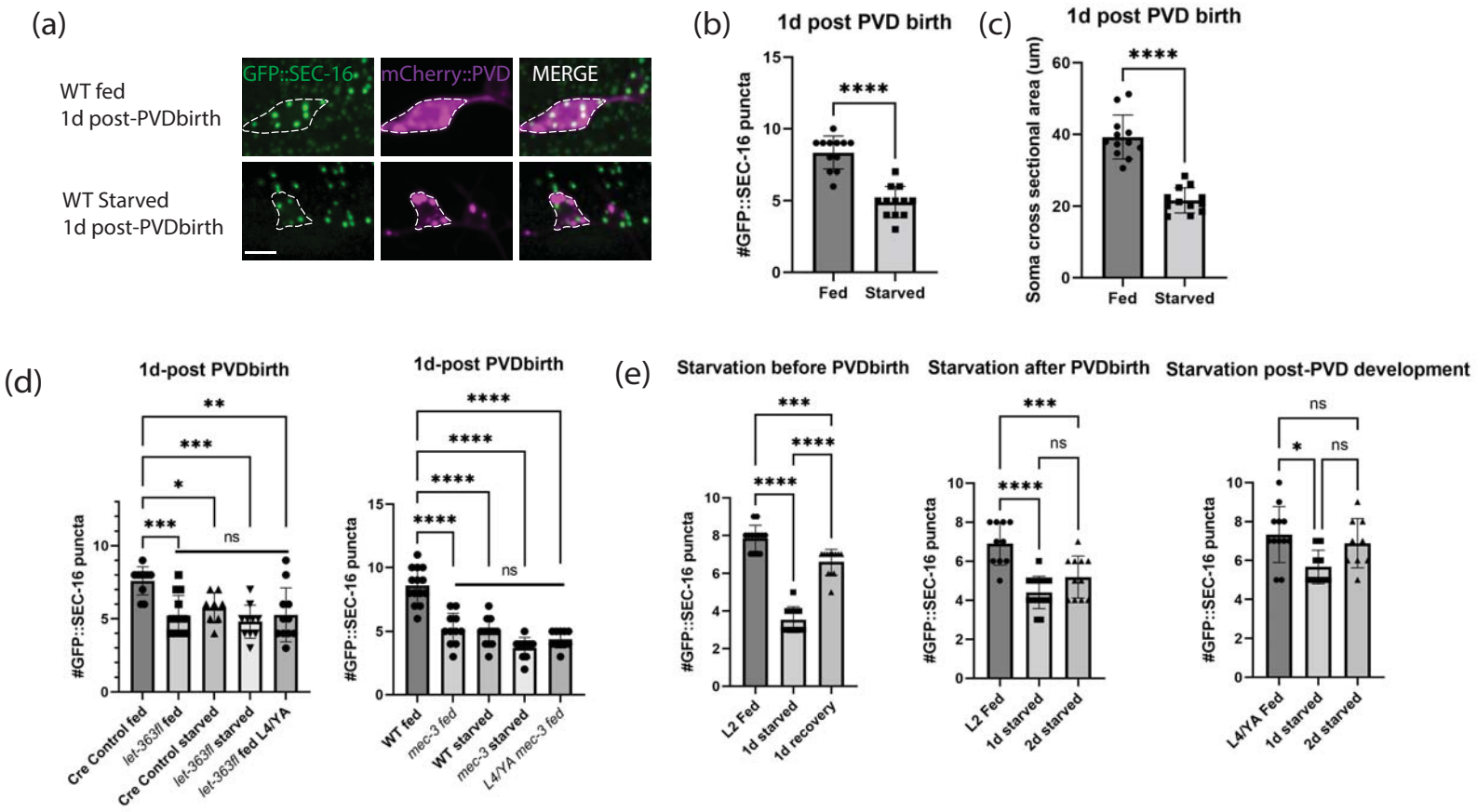

Fig. 6: Stage-specific nutrient deprivation reduces PVD ERES number. (a) Confocal fluorescence microscopy close-ups of PVD soma and endogenous ERES marker, GFP::SEC-16, one day after PVD birth in fed or 1-day starved wildtype animals (scale bar = 5µm). PVDs in fed and starved animals were quantified for (b) number of GFP::SEC-16 puncta, and (c) soma size estimated as described in methods. (d) Number of GFP::SEC-16 puncta of fed vs starved animals in wildtype vs *mec-3* (left) and Cre-control vs *let-363*-floxed animals (right). (e) Number of GFP::SEC-16 puncta in wildtype animals removed from nutrients at different stages of PVD development, and starved for either one day and recovered (left), or two days (middle and right). Significance determined by one-way ANOVA, *p<.05,***p<.001, ****p<.0001.

Table S1:

Strain ID	Genotype
TV27272	sec-16a.2(wy1524) wyIs900 X; wyIs891 III; wyIs581 IV
TV28411	wyEx10586; sec-16a.2(wy1524) X; wyIs969 IV?
TV28412	wyEx10587; sec-16a.2(wy1524) X; wyIs969 IV?
TV27277	*ahr-1(ju145)* I; sec-16a.2(wy1524) wyIs900 X; wyIs891 III
TV26984	wyEx10309; wyEx9857; wyIs592 III
TV24562	wyEx9857; wyIs592 III
TV27727	wyEx10429; wyIs581 IV; sec-16a.2(wy1524) wyIs900 X
TV27728	wyEx10429; mec-3(e1338) wyIs581 IV; sec-16a.2(wy1524) wyIs900 X
TV26084	wyIs50030
TV26063	*hpo-30(ok2047)*;wyIs50030
TV26064	*kpc-1(gk8)*; wyIs50030
TV26073	*dma-1(tm5159)*; wyIs50030
TV26068	*unc-86(e1416)*; wyIs50030
TV27747	*sec-16a.2(wy1524)* wyIs900 X; *lin-5(wy1576)* II; *zif-1(gk117)* III; wyIs581 IV
TV27812	wyEx9744; *lin-5(wy1576)* II; zif-1(gk117) III; wyIs969 (IV?); *sec-16a.2(wy1524)* wyIs900 X
TV27272	sec-16a.2(wy1524)/wyIs900 X; wyIs891 III; wyIs581 IV
TV27776	let-363(ok3018)/hT2 I; sec-16a.2(wy1524) wyIs900 X; wyIs891 III; wyIs581 IV
TV28329	let-363[floxed atg + first 8 exons](wy1706) I; wyIs901 wyIs592 III
TV27845	wyIs897 X? sec-16a.2(wy1524) X; wyIs969 IV? wyIs581 IV
TV28418	wyIs897 sec-16a.2(wy1524) X; let-363[floxed atg + 8 exons](wy1706) I; wyIs969 wyIs581 IV
WT plet-363::GFP	Crossed from FR297[22]. rol-6(n1276e187); swEx226 [rol-6(su1006) let-363/tor::gfp]; sec-16a.2(wy1524) wyIs900 X; wyIs581 IV
mec-3 (e1338) plet-363::GFP	rol-6(n1276e187); swEx226 [rol-6(su1006) let-363/tor::gfp]; sec-16a.2(wy1524) wyIs900 X; wyIs581 IV

Mutant alleles	Notes
sec-16a.2(wy1524) X	CRISPR inserted AID::GFP::N-terminal_FRTonCassette(FRTminimal::Degron::STOP::FRTminimal) fused at the 3' of endogenous *sec-16A.2*
ahr-1(ju145)	obtained from CGC
sec-16a.2(wy1750)[GFP::FRT::Degron::STOP::FRT::sec-16a.2] X	CRISPR removed AID from sec-16a.2(wy1524)
lin-5(wy1576) II	lin-5::ZF knock in

let-363(ok3018)	(ortholog of mTOR) arrests during larval development in L3-early L4. Obtained from CGC
mec-3(e1338)	obtained from CGC
unc-86(e1416)III	obtained from CGC
hpo-30(ok2047)	
kpc-1(gk8)	
dma-1(tm5159)	
let-363(wy1706)	CRISPR added loxp sites. First loxp site is just after the closest upstream gene at the beginning of the putative let-363 promoter. The other loxP site is in the long intron after the 8th exon

Integrated transgenes		
allele	constructs for injection	notes
wyIs900 X	plin-32>mCherry::PH(PLCδ) (pJL188, 1ng/µl) + punc-122>RFP (60ng/µl)	Integrant of wyEx9914 in ChrX
wyIs891 III	Punc-86::FLP (pDML63) 5ng/ul, 100 ng/ul Podr-1::RFP	Flippase (FLP) is used to excise FRT cassettes for cell-specific endogenous tagging of selected genes with XFP/tag
wyIs581 IV	ser2prom3::myrmCherry::unc-54 3'UTR (pOL036), with Podr-1::GFP	
wyIs969 IV?	plin-32::FLP (@5ng/ul) with podr-1::RFP (@60ng/ul). >6x outcrossed	Integrant of wyEx10429, probably on IV
wyIs592 III	ser2prom3::myr-GFP(pOL020, 20ng/ul)+Podr-1::RFP.	Integrant of wyEx3355, on chromosome III
iesi57	[eft-3p::TIR1::mRuby::unc-54 3'UTR + Cbr-unc-119(+)] II	Single copy transgene inserted into chromosome II (oxTi179) expressing modified Arabidopsis thaliana TIR1 tagged with mRuby in the soma. This strain can be used for auxin-inducible degradation (AID) in somatic tissues. Reference: Zhang L, et al. Development. 2015 Nov 9. pii: dev.129635.
wyIs836	Integrant of Pnhr-81::FLP (pDML60) 2.5ng/ul, 100 ng/ul Podr-1::RFP.	Flippase (FLP) is used to excise FRT cassettes for cell-specific endogenous tagging of selected genes with XFP/tag

wyIs50030	pPD95.77_ser-2Prom3::aman-2::GFP(2ng/ul) ser-2P3::mCherry(5ng/ul) Podr-1::GFP(50ng/ul)	
wyIs901	pnhr-81::cre + punc-122::rfp	Integrant of wyEx8881 on III
wyIs897	pnhr-81::cre + punc-122::rfp	integrant of wyEx8881, probably on X

allele	Constructs	notes
wyEx10586	Pmec-17::mscarlet(plasmid KE51) (1ng/ul); Podr-1::GFP (40ng/ul)	expresses mscarlet in touch receptor neurons
wyEx10429	plin-32::FLP (@5ng/ul) with podr-1::RFP (@60ng/ul)	Flippase (FLP) is used to excise FRT cassettes for cell-specific endogenous tagging of selected genes with XFP/tag
wyEx10587	FLP, PVD>mScarlet (Chris Tzeng plasmid @ 0.5 ng/uL); Punc-122::RFP (30ng/ul)	This array labels PVD and FLP in red
wyEx10309	Pser2prom3::sar-1-DN(dominant negative) (pCER218 @ 4ng/ul); Pmyo2::GFP @ 2ng/ul	
wyEx9857	ser2prom3::sec-23::tagrfp, Pmyo-2::rfp.	
wyEx9744	pMK41 (punc-86::mCherry::PLCdeltaPH) @ 2.5 ng/ul + pMK32 (punc-86::zif-1) @ 2.5 ng/ul + Podr-1::gfp @ 30 ng/ul	expresses zif-1 in PVDmother (for degradation of lin-5)
wyEx10429	plin-32::FLP (@5ng/ul) with podr-1::RFP (@60ng/ul)	Flippase (FLP) is used to excise FRT cassettes for cell-specific endogenous tagging of selected genes with XFP/tag
swEx226	swEx226 = [rol-6(su1006) + let-363/tor::gfp] Made by injecting 50 ug/ml pG70.3 and 200 g/ml pRF4 rol-6(su1006) 18	Originally from FR297[22]